

Adaptive Superpixel Cuts for Hyperspectral Images

Aleksandar Popovic

Supervised by Dr. You Liang & Dr. Na Yu

Abstract

Blind segmentation in hyperspectral images is a challenging problem. Many traditional methods suffer from poor identification of materials and expensive computational costs, which can be partially eased by trading the accuracy with efficiency.

In this paper, we propose a novel graph-based algorithm for segmentation in hyperspectral images. Utilizing the fact that pixels in a local region are likely to have similar spectral features, a pre-clustering algorithm is used to extract the homogeneous regions, called superpixels. After extracting the superpixels, a weighted graph is constructed with the weights representing both the spectral similarity and spatial distance between each superpixel and its neighbors. The normalized graph cuts algorithm is then used to perform an initial segmentation of the image. To effectively extract the material information in the superpixels, the mean spectra in each segment is used to estimate the abundance of each endmember in each superpixel using a graph regularized hyperspectral unmixing algorithm. The resulting abundance information is used as a supportive feature, which when combined with the spectral features, form a new spectral feature vector for each superpixel. Using this new feature vector, the weighted graph is once again constructed and the normalized cuts algorithm is applied, resulting in a final segmentation of the image.

Experiments on a real hyperspectral datasets illustrate great potential of the proposed method in terms of accuracy and efficiency.

Acknowledgements

Words cannot express my gratitude to my supervisors Dr. You Liang and Dr. Na Yu for their invaluable guidance over the past two years. They were the best providers of constructive feedback and mentors I could ask for. They helped me develop not only my research skills but also my critical thinking and problem-solving abilities. Their advice and encouragement will continue to be valuable assets in my future endeavors.

Thank you to our experimental collaborators, Dr. Yeni Yucel and his Ophthalmic Pathology lab at St. Michaels Hospital for providing the motivation in developing this work.

I'd like to thank my family and friends for their support every step of the way. I would also like to thank my grandfather for instilling the importance of lifelong education at a young age.

Contents

1	Introduction	4
2	Background	5
2.1	The Hyperspectral Cube	5
2.2	Superpixel Generation	5
2.2.1	Simple Linear Iterative Clustering	5
2.3	Hyperspectral Unmixing	6
2.3.1	Linear Mixing Model	6
2.3.2	Abundance Estimation	6
2.4	Alternating Direction Method of Multipliers	7
2.5	Spectral Clustering	8
2.5.1	Normalized Cuts	9
3	Adaptive Superpixel Cuts	10
3.1	Dataset Preprocessing	10
3.2	Hyperspectral Superpixel Generation	10
3.3	Spatial Spectral Clustering	11
3.4	Graph Regularized Abundance Estimation	12
3.5	Feature Vector Creation	16
3.6	Algorithm Overview	17
4	Experimental Results	18
4.1	Evaluation Datasets	18
4.2	Algorithm Evaluation	21
4.2.1	Quantitative Evaluation on Salinas	21
4.2.2	Qualitative Evaluation on Samson	23
5	Conclusions	25

1 Introduction

The realm of image analysis has witnessed a significant revolution with the advent of hyperspectral imaging technology. Unlike traditional cameras that capture data in just a few broad spectral bands (e.g., red, green, blue), hyperspectral sensors record information across hundreds of contiguous spectral bands. This remarkable capability allows for the creation of detailed "spectral fingerprints" for each pixel in an image. These fingerprints unveil the unique spectral characteristics of materials present within the scene, offering invaluable insights in diverse fields like remote sensing, material identification, and environmental monitoring.

Extracting meaningful information from hyperspectral images, however, presents a unique challenge. The sheer volume of data, with each pixel containing hundreds of spectral values, necessitates sophisticated image analysis techniques for effective interpretation. Image segmentation is a image processing approach that aims to group pixels with similar characteristics into distinct regions. In the context of hyperspectral images, this translates to grouping pixels with identical or very similar spectral signatures, effectively creating regions that represent objects or materials of interest within the scene. By segmenting the image, researchers can isolate and analyze specific materials, track their distribution, and ultimately gain deeper understanding of the observed environment.

Traditional image segmentation methods have been employed for hyperspectral data analysis with varying degrees of success. Common approaches include unsupervised clustering techniques, which group pixels based on their spectral similarity without any prior knowledge about the scene. Additionally, supervised classification algorithms can be utilized when labeled training data is available. These methods learn from pre-labeled examples to classify pixels into predefined categories. However, these existing methods have limitations when dealing with the complexities of hyperspectral data. High dimensionality of the data, with hundreds of spectral bands, can pose computational challenges for traditional algorithms. Moreover, the presence of mixed pixels, where a single pixel contains contributions from multiple materials, can lead to inaccurate segmentation results. Lastly, some methods struggle to handle situations where spectrally similar materials are present in spatially distinct locations within the image. These limitations highlight the need for efficient and accurate unsupervised segmentation approaches that can effectively address the unique characteristics of hyperspectral data.

2 Background

Analysis in hyperspectral images has traditionally been a computationally expensive and difficult task due to algorithms scaling in both the spatial and spectral resolution of the images. This section will focus on building a relevant background for common preclustering, abundance estimation, and segmentation techniques from the perspective of imaging that will be later adapted for use in the proposed algorithm.

2.1 The Hyperspectral Cube

Traditional RGB images are images that can be represented by a 3-dimensional tensor of shape $(n_x, n_y, 3)$, where the last dimension corresponds to the three color channels the image was captured in. From a mathematical point of view, a hyperspectral image, denoted by \mathbf{X} , is a tensor of shape (n_x, n_y, n_λ) with nonnegative entries. Each pixel in the tensor is represented using a vector $\mathbf{x} \in \mathbb{R}_+^{n_\lambda}$. From a physical point of view, the first two dimensions in \mathbf{X} represent the spatial coordinates of the pixels, while the last dimension represents the band the spectral intensity, reflectance, or transmittance measurements were taken at.

2.2 Superpixel Generation

As mentioned in Section (2.1), high spectral resolution is a both an advantage and a challenge in hyperspectral image analysis, which causes the time complexity of certain algorithms to scale polynomially with the number of pixels in the image.

Before the introduction of neural network based solutions in computer vision applications, there was interest in preclustering images into locally homogeneous regions called superpixels (Achanta et al., 2012). Addressing the main motivation of reducing the overall granularity of the data, superpixels are also shown to preserve spectral information, adhere to spatial features in the image, and introduce robustness against noise in subsequent analysis tasks.

2.2.1 Simple Linear Iterative Clustering

In this section, we will introduce the Simple Linear Iterative Clustering (SLIC) algorithm. The algorithm is a special case of the k-means algorithm adapted to the task generating superpixels for images in the 3-dimensional CIELAB color space, where each pixel (i, j) is represented as $\mathbf{x}_{(i,j)} = [x_l, x_a, x_b]$.

Taking as an input the desired number of superpixels n_s , for an image with $n_p = n_x n_y$ pixels, each superpixel would be composed of approximately n_s/n_p pixels. Assuming the superpixels lie on a grid, a superpixel centroid would occur at every grid interval $S = \sqrt{n_s/n_p}$. At the onset of the algorithm, a grid of n_s superpixel centers $\mathbf{c}_n = [c_l, c_a, c_b]$ where $n = 1, \dots, n_s$ are sampled across the image with regular grid intervals S . To avoid sampling noisy pixels, clusters are moved to the lowest gradient position in a 3×3 neighborhood where the image gradient is calculated, using the original spectral vector \mathbf{x} in the CIELAB color space:

$$\mathbb{G}(i, j) = \|\mathbf{x}_{(i+1,j)} - \mathbf{x}_{(i-1,j)}\|^2 + \|\mathbf{x}_{(i,j+1)} - \mathbf{x}_{(i,j-1)}\|^2 \quad (1)$$

After initialization, a modified distance measure is proposed to enforce color similarity and spatial extent within the superpixels. Since the approximate area of each superpixel is S^2 , it is assumed that pixels associated with a superpixel lie within a $2S \times 2S$ neighborhood of the superpixel centroid. Introducing the parameter m to control the compactness and shape of the superpixels, the modified distance is then calculated as

$$\mathbb{D}(\mathbf{x}, \mathbf{c}_n) = \|\mathbf{x} - \mathbf{c}_n\|_2^2 + \frac{m}{S} d_{\text{spatial}}(\mathbf{x}, \mathbf{c}_n)^2 \quad (2)$$

Each pixel in the image is associated with the nearest cluster whose search area overlaps this pixel. After all pixels are associated with a cluster, a new center is computed as the average feature vector of all the pixels belonging to the cluster. This is repeated for a set number of iterations k_{max} . At completion, the final superpixelized image is given by arranging the feature vectors into columns of the matrix $\mathbf{C} = [\mathbf{c}_1 \mid \mathbf{c}_2 \mid \dots \mid \mathbf{c}_{n_s}] \in \mathbb{R}^{3 \times n_s}$.

Algorithm 1: SLIC Superpixel Algorithm

Input:

CIELAB Image \mathbf{X} $m > 0, n_s > 0, k_{\max} > 0$

Initialize: $\mathbf{c}_n = [c_l, c_a, c_b]$ where $n = 1, \dots, n_s$ by sampling pixels at regular grid intervals S . Perturb cluster centers to lowest gradient position in a 3×3 neighborhood according to (1)

for $k = 1$ **to** k_{\max} **do**

 Assign best matching pixels from a $2S \times 2S$ neighborhood around clusters $\mathbf{c}_1, \mathbf{c}_2, \dots, \mathbf{c}_{n_s}$ according to (2).

 Compute new cluster centers according to average vector of all pixels belonging to cluster.

end

Output: Superpixelated Image Matrix $\mathbf{C}_s = [\mathbf{c}_1, \mathbf{c}_2, \dots, \mathbf{c}_{n_s}]$

The SLIC algorithm is shown to produce meaningful and noise-robust segments in traditional computer vision applications. This algorithm proves its function in denoising and dimension reduction in Section 3.2 when adapted as a spatial preprocessing step in the hyperspectral domain.

2.3 Hyperspectral Unmixing

In hyperspectral imaging applications, spectral unmixing emphasizes estimating the relative abundance of a given representative material, called an endmember, within each pixel. Unmixing results often give more detailed information about the overall composition of a hyperspectral scene with a set of selected endmembers. This section will introduce the foundational knowledge behind unmixing and abundance estimation.

2.3.1 Linear Mixing Model

In reality, most pixels in a hyperspectral image capture a mixture of spectra reflected from various materials present within the spatial area, due to constraints with how large a spatial resolution can be achieved. The foundational model behind hyperspectral unmixing is the linear mixing model, which dictates that spectra of every pixel $\mathbf{x} \in \mathbb{R}_+^{n_\lambda}$ in a hyperspectral image is a linear combination of a set of n_e spectra, $\mathbf{m}_1, \mathbf{m}_2, \dots, \mathbf{m}_{n_e} \in \mathbb{R}_+^{n_\lambda}$, from pure representative materials, called endmembers, with weights $a_1, a_2, \dots, a_{n_e} \in \mathbb{R}$. Denoting $\mathbf{M} = [\mathbf{m}_1 \mid \mathbf{m}_2 \mid \dots \mid \mathbf{m}_{n_e}] \in \mathbb{R}_+^{n_\lambda \times n_e}$ and $\mathbf{a} = [a_1, a_2, \dots, a_{n_e}]^T \in \mathbb{R}^{n_e}$, the linear mixing model is formulated as follows:

$$\mathbf{x} = \mathbf{M}\mathbf{a} + \epsilon \quad (3)$$

While this unconstrained model serves useful to unmixing an image, there is no direct physical interpretation to the weights in \mathbf{a} . Instead, we aim to estimate the physical proportion, called the abundance, of each endmember within each pixel by imposing two constraints on the entries in \mathbf{a} . The abundance nonnegativity constraint (ANC) requires that the entries in \mathbf{a} must be greater than or equal to zero, while the abundance sum-to-one constraint (ASC) requires that the entries in \mathbf{a} sum to 1 (Keshava and Mustard, 2002). Combining the two constraints, we have an extension of the linear mixing model

$$\mathbf{x} = \mathbf{M}\mathbf{a} + \epsilon \quad \text{s.t. } \mathbf{a} \in \mathbb{R}_+^{n_e} \text{ and } \|\mathbf{a}\|_1 = 1 \quad (4)$$

The linear mixing model can be additionally be extended from a per pixel basis onto a collection of n_p pixels $\mathbf{X} = [\mathbf{x}_1 \mid \mathbf{x}_2 \mid \dots \mid \mathbf{x}_{n_p}] \in \mathbb{R}_+^{n_\lambda \times n_p}$, with each pixel \mathbf{x}_i having a corresponding abundance vector \mathbf{a}_i . Arranging the abundance vectors into an abundance matrix $\mathbf{A} = [\mathbf{a}_1 \mid \mathbf{a}_2 \mid \dots \mid \mathbf{a}_{n_p}] \in \mathbb{R}^{n_e \times n_p}$, we denote the ANC-ASC constraint using the set $\Delta = \{\mathbf{A} \in \mathbb{R}_+^{n_e \times n_p} \mid \mathbf{1}_{n_e}^T \mathbf{A} = \mathbf{1}_{n_p}\}$. The following natural extension of the linear mixing model to a collection of pixels will be the base for the following sections

$$\mathbf{X} = \mathbf{M}\mathbf{A} + \epsilon \quad \text{s.t. } \mathbf{A} \in \Delta \quad (5)$$

The linear mixing model ((5)) is an simplistic model, which enforces a linear relationship between the spatial mixing of endmembers through assuming that pixels lie on a flat plane, as such, pixel measurements are dictated by how much each endmember is present. The model itself remains a efficient and powerful tool for extracting spectral information from a scene, even in modern analysis.

2.3.2 Abundance Estimation

Given the linear mixing model ((5)), in traditional hyperspectral imaging tasks, both \mathbf{M} and \mathbf{A} are unknown. Often, researchers aim to estimate \mathbf{M} first, as spectral signatures collected from endmembers in same scene under the same

conditions will be almost identical. Notably, in the field of remote sensing, effort has been made to create a library of spectral signatures derived from common vegetation and minerals in land cover images, allowing focus to be made solely in estimating \mathbf{A} (Meerdink et al., 2019). This section will cover the scenario where \mathbf{M} is known and \mathbf{A} is to be estimated. The task is referred to as abundance estimation and continues to be an active area of research, where the aim is to find \mathbf{A} such that an error function \mathcal{L} is minimized with respect to the reconstructed collections of pixels $\tilde{\mathbf{X}} = \mathbf{MA}$ and the original collection of pixels \mathbf{X} . Traditionally, we aim to minimize the least-square reconstruction error between the entries in $\tilde{\mathbf{X}}$ and \mathbf{X}

$$\mathcal{L}(\mathbf{X}, \tilde{\mathbf{X}}) = \sum_{i=1}^{n_\lambda} \sum_{j=1}^{n_p} (\mathbf{x}_{(i,j)} - \tilde{\mathbf{x}}_{(i,j)})^2 = \|\tilde{\mathbf{X}} - \mathbf{X}\|_F^2 \quad (6)$$

The least-squares reconstruction error can alternatively be written as the squared Frobenius norm, denoted as $\|\cdot\|_F^2$, of the difference between $\tilde{\mathbf{X}}$ and \mathbf{X} . This choice of \mathcal{L} is the straight forward and natural approach as \mathcal{L} is both convex and differentiable, with the additional properties that $\mathcal{L}(\tilde{\mathbf{X}}, \mathbf{X}) = \mathcal{L}(\mathbf{X}, \tilde{\mathbf{X}})$ and $\mathcal{L}(\mathbf{X}, \tilde{\mathbf{X}}) = \mathcal{L}(\mathbf{X}^T, \tilde{\mathbf{X}}^T)$ (Keshava and Mustard, 2002).

To incorporate the ANC-ASC constraint into the overall formulation of \mathcal{L} , the set Δ from Section 2.3.1 plays a significant role. It is important to note that Δ is a convex set, meaning that for matrices $A, B \in \Delta$, for all $0 \leq \alpha \leq 1$, the matrix $C = \alpha A + (1 - \alpha)B$ is also an element of Δ . The inclusion of the constraints on \mathbf{A} is facilitated using the piece wise function χ_S defined as follows

$$\chi_S(x) = \begin{cases} 0 & \text{if } x \in S \\ \infty & \text{if } x \notin S \end{cases} \quad (7)$$

Adding χ_Δ in the formulation of \mathcal{L} restricts the values \mathbf{A} can take on to the set Δ , while ensuring that the overall formulation still has a global minimum within Δ . Additionally, a regularization term J can be added to impose additional constraints on the values in \mathbf{A} . Formally, abundance estimation can be formulated as a convex optimization problem of the form

$$\hat{\mathbf{A}} = \arg \min_{\mathbf{A} \in \mathbb{R}^{n_e \times n_p}} \frac{1}{2} \|\mathbf{MA} - \mathbf{X}\|_F^2 + \chi_\Delta(\mathbf{A}) + J(\mathbf{A}) \quad (8)$$

This problem has no closed form solution, relying on iterative methods or applying solvers to solve the problem for individual pixels given the problem can be split pixel wise. The formulation of the abundance estimation problems allows for additional image specifications to be added depending on the domain of research.

2.4 Alternating Direction Method of Multipliers

Alternating Direction Method of Multipliers, or ADMM, introduced in (Boyd et al., 2011), is a framework for solving convex optimization problems of the form:

$$\begin{aligned} & \text{minimize} && f(x) + g(z) \\ & \text{subject to} && Ax + Bz = c \end{aligned} \quad (9)$$

with variables $x \in \mathbb{R}^n$ and $z \in \mathbb{R}^m$, where $A \in \mathbb{R}^{p \times n}$, $B \in \mathbb{R}^{p \times m}$ and $c \in \mathbb{R}^p$. f and g are assumed to be convex. The aim of ADMM is to incorporate the decomposability of the dual ascent method into the superior convergence properties of method of multipliers. To allow for this, ADMM introduces the corresponding augmented Lagrangian \mathcal{L}_μ defined as:

$$\mathcal{L}_\mu(x, z, y) = f(x) + g(z) + y^T(Ax + Bz - c) + \frac{\mu}{2} \|Ax + Bz - c\|_2^2 \quad (10)$$

where $\mu > 0$ is augmented Lagrangian convergence parameter and $y \in \mathbb{R}^p$ is the corresponding dual variable. Scaling with $u = \frac{1}{\mu}y$ gives the following equivalent definition:

$$\mathcal{L}_\mu(x, z, u) = f(x) + g(z) + \frac{\mu}{2} \|Ax + Bz - c + u\|_2^2 \quad (11)$$

ADMM aims to minimize scaled form of \mathcal{L}_μ by alternating minimizations with respect to x , y , and u by performing the following updates:

$$\begin{aligned}
x^{(k+1)} &= \arg \min_x \mathcal{L}_\mu(x, z^{(k)}, u^{(k)}) \\
z^{(k+1)} &= \arg \min_z \mathcal{L}_\mu(x^{(k+1)}, z, u^{(k)}) \\
u^{(k+1)} &= u^{(k)} + Ax^{(k+1)} + Bz^{(k+1)} - c
\end{aligned} \tag{12}$$

Under mild conditions on f and g , ADMM can be shown to provide guaranteed objective and residual convergence, independent on choice of μ . For lax choices of μ , the algorithm provides modest accuracy solutions in a relatively low number of iterations, favorable to tasks in statistical learning where parameter estimation often yields little improvement to results. The algorithm allows practitioners to put focus on efficient implementations to the minimization problems for x and z , and not on parameter tuning.

2.5 Spectral Clustering

Clustering aims to partition unlabelled data into a set of groupings called clusters such that a predefined similarity metric is minimized within the data points in the cluster and maximized between clusters. Traditional clustering methods such as k-means, and tree based methods suffer in situations where both spatial and spectral information must be taken into account for computing clusters and often are sensitive to initialization and outliers in data. The focus of this section is to introduce the concept of spectral clustering, which aims to partition a set of data points into cluster by storing similarity between data points in a graph structure then using spectral analysis techniques to calculate globally optimal partitions.

The particular focus will be in the context of imaging, and particularly hyperspectral imaging, and the final product of a clustering algorithm should be perceptually meaningful groupings that respect both the spectral and spatial features in the image. Considering a collection of pixels $\mathbf{X} = [\mathbf{x}_1 \mid \mathbf{x}_2 \mid \cdots \mid \mathbf{x}_{n_p}] \in \mathbb{R}_+^{n_\lambda \times n_p}$ and defining a symmetric similarity measure d , the affinity matrix $\mathbf{W} \in \mathbb{R}_+^{n_p \times n_p}$ is constructed as

$$\mathbf{W}_{(i,j)} = d(\mathbf{x}_i, \mathbf{x}_j) \tag{13}$$

Typical choices for d in imaging applications include calculating the euclidean norm and the cosine angle between the spectral features of \mathbf{x}_i and \mathbf{x}_j . The euclidean distance calculates the difference in magnitude between the two pixels, leading to sensitivity under different lighting conditions. Cosine angle calculates the relative angle between the two pixel vectors, with 0 indicating that the pixels are exactly identical or one of them is a scaled version of the other. Cosine angle is often the metric of choice due to its scale invariance property, allowing for better distinction of materials in different lighting conditions.

$$\begin{aligned}
d_{L_2}(\mathbf{x}_i, \mathbf{x}_j) &= \|\mathbf{x}_i - \mathbf{x}_j\|_2 \\
d_\theta(\mathbf{x}_i, \mathbf{x}_j) &= \arccos \left(\frac{\mathbf{x}_i \mathbf{x}_j^T}{\|\mathbf{x}_i\|_2 \|\mathbf{x}_j\|_2} \right)
\end{aligned} \tag{14}$$

As $d_{L_2} \in [0, \infty)$ and $d_\theta \in [0, \pi]$, the affinity matrix \mathbf{W} can alternatively be constructed using the heat kernel matrix with $0 < \sigma < 1$, this pushes similar pixels to have $\mathbf{W}(i, j) = 0$ and dissimilar pixels to have $\mathbf{W}(i, j) = 1$.

$$\mathbf{W}_{(i,j)} = \exp \left(-\frac{d(\mathbf{x}_i, \mathbf{x}_j)^2}{\sigma^2} \right) \tag{15}$$

A graph $G = (V, E)$ is a set of vertices V and edges E that connect them. Considering the set of pixels $\{\mathbf{x}_1, \mathbf{x}_2, \dots, \mathbf{x}_{n_p}\}$ as the set of vertices and $d(\mathbf{x}_i, \mathbf{x}_j)$ as the edges between them, \mathbf{W} is the matrix representation of an undirected weighted graph G_W . Spectral Analysis is then the study of \mathbf{W} using linear algebra techniques to determine insights on the structure of G_W using the eigenvalues and eigenvectors of \mathbf{W} . A fundamental matrix in spectral analysis is the graph Laplacian matrix \mathbf{L} , calculated as the difference between the diagonal matrix \mathbf{D} where

$$\mathbf{D}_{(i,j)} = \begin{cases} \sum_j \mathbf{W}_{(i,j)} & \text{if } i = j, \\ 0 & \text{if } i \neq j \end{cases} \tag{16}$$

and \mathbf{W} . Formally,

$$\mathbf{L} = \mathbf{D} - \mathbf{W} \tag{17}$$

As \mathbf{L} is known to be positive semidefinite, the eigenvalues $\lambda_1, \lambda_2, \dots, \lambda_n$ are strictly non-negative and provide key insights into the structure of G .

2.5.1 Normalized Cuts

A graph $G = (V, E)$ with affinity matrix \mathbf{W} can be partitioned into two subgraphs $G_A = (V_A, E_A)$ and $G_B = (V_B, E_B)$ such that $V_A \cup V_B = V$ and $V_A \cap V_B = \emptyset$ by removing the edges between the vertices in G_A and G_B . The dissimilarity between these two graphs can be calculated as the sum of the edges cut to form the partitions

$$\text{cut}(G_A, G_B) = \sum_{i \in V_A, j \in V_B} \mathbf{W}_{(i,j)} \quad (18)$$

The optimal bi-partitioning of G_W is given as the graphs G_A and G_B that minimize (18). However, in the case of image segmentation, this criteria will heavily prioritize partitioning single pixels from the image. Instead, the normalized cuts criteria is proposed, focusing on balancing the ratio between the edges cut and the sum of the internal edge nodes within G_A and G_B defined as

$$\text{ncut}(G_A, G_B) = \frac{\text{cut}(G_A, G_B)}{\text{assoc}(G_A, G)} + \frac{\text{cut}(G_A, G_B)}{\text{assoc}(G_B, G)} \quad (19)$$

where

$$\text{assoc}(G_A, G) = \sum_{i \in V_A, j \in V} \mathbf{W}_{(i,j)} \quad (20)$$

The normalized cuts criteria, in general terms, aims to minimize the disassociation between the subgraphs and maximize the association within them. While (19) is NP-Complete, (Shi and Malik, 2000) show that solving for the eigenvector \mathbf{u}_2 corresponding to the second smallest eigenvalue λ_2 in the system

$$\mathbf{D}^{-\frac{1}{2}}(\mathbf{D} - \mathbf{W})\mathbf{D}^{-\frac{1}{2}}\mathbf{z} = \lambda\mathbf{z} \quad (21)$$

provides a approximate real valued solution to (19) through assigning subgraph membership of the vertices according to the sign of the entries in \mathbf{u}_2 .

Spectral graph techniques like the normalized cuts algorithm provide the advantage of flexible and deterministic results based on the initialization of the adjacency matrix \mathbf{W} , however begin to fall behind iterative methods when the graph is large, due to the time complexity of solving (21) scaling cubically with the number of vertices.

3 Adaptive Superpixel Cuts

This section focuses on introducing the proposed unsupervised hyperspectral image segmentation algorithm, Adaptive Superpixel Cuts for Hyperspectral Images (ASC-HSI). This segmentation algorithm for hyperspectral images presents a two-stage approach that addresses challenges in hyperspectral data analysis. Unlike traditional methods that operate directly on every pixel, this algorithm leverages a clever step of pre-segmenting the image into small, uniform regions called superpixels. This initial segmentation based on spectral similarity of each small local region offers a significant runtime advantage. By focusing on these superpixels instead of individual pixels, the algorithm reduces the computational complexity involved in subsequent processing stages. The second stage refines the segmentation by incorporating the estimated abundance of different materials within each superpixel region. This combination of efficient superpixel processing and material abundance estimation offers potential advantages in accuracy, particularly for handling mixed pixels and spectrally similar materials in distinct locations.

3.1 Dataset Preprocessing

As mentioned in Section 2.1, the input to the algorithm is a hyperspectral image represented by a nonnegative tensor $\mathbf{X} \in \mathbb{R}_+^{n_x \times n_y \times n_\lambda}$. Raw hyperspectral images are susceptible to outliers and scale invariance across wavelengths. As such, to ensure algorithms perform reliably along a wide range of domains, preprocessing is a crucial step. Typically, the first main goal of practitioners is to deal with noise and regularization across the spectral dimension, then work to deal with spatial artifacts in the image. Hyperspectral images have a wide range of bands; therefore, some bands have significantly higher intensities compared to others. It is important to consider the full collection of wavelengths rather than allow the over prioritization of higher intensity wavelengths, especially in situations where direct scale comparison is made between pixels. By normalizing each spectral band to a similar scale, all spectral bands contribute more equally to the segmentation process. This ensures that results capture the underlying spectral information more effectively. A common approach to normalization in hyperspectral images is band normalization, where intensity values for the hyperspectral image at spectral band k , denoted $\mathbf{X}_{(:,\cdot,k)}$ are independently scaled to a range $[0, 1]$ according to the minimum and maximum values at that band. Formally,

$$\hat{\mathbf{X}}_{(:,\cdot,k)} = \frac{\mathbf{X}_{(:,\cdot,k)} - \min \mathbf{X}_{(:,\cdot,k)}}{\max \mathbf{X}_{(:,\cdot,k)} - \min \mathbf{X}_{(:,\cdot,k)}} \quad (22)$$

3.2 Hyperspectral Superpixel Generation

In 2.2.1, the SLIC algorithm was introduced, aiming to perceptually group pixels into locally homogeneous groups called superpixels. While the SLIC algorithm was originally developed for use in the CIELAB color space, a similar methodology can be applied towards the hyperspectral space. The main modification when transitioning to the hyperspectral domain requires the consideration of all the spectral features.

With the preprocessed hyperspectral image $\hat{\mathbf{X}}$, each pixel is represented by the vector $\hat{\mathbf{x}}_{(i,j)} = [\hat{x}_1, \hat{x}_2, \dots, \hat{x}_{n_\lambda}]$. Then, taking as an input the number of superpixels n_s , superpixel centroids $\mathbf{c}_n = [c_1, c_2, \dots, c_{n_\lambda}]$ where $n = 1, \dots, n_s$ are created at regular grid intervals $S = \sqrt{n_s/n_p}$ across the image. The initial centroids are moved to the lowest gradient position in a 3×3 spatial neighborhood where the image gradient is now calculated using the original hyperspectral features instead of the CIELAB features:

$$\mathbb{G}(i, j) = \|\hat{\mathbf{x}}_{(i+1,j)} - \hat{\mathbf{x}}_{(i-1,j)}\|_2^2 + \|\hat{\mathbf{x}}_{(i,j+1)} - \hat{\mathbf{x}}_{(i,j-1)}\|_2^2 \quad (23)$$

Following the original formulation of the SLIC algorithm, a modified distance measure is proposed to enforce color similarity and spatial extent within the superpixels. Using the same parameter m to control the compactness and shape of the superpixels, the modified distance between a pixel $\hat{\mathbf{x}}$ and cluster \mathbf{c}_n is now calculated as L_2 difference between the spectral features plus a scaled version of the spatial euclidean distance between the pixel and the cluster center:

$$\mathbb{D}(\hat{\mathbf{x}}, \mathbf{c}_n) = \|\hat{\mathbf{x}} - \mathbf{c}_n\|_2^2 + \frac{m}{S} d_{\text{spatial}}(\hat{\mathbf{x}}, \mathbf{c}_n)^2 \quad (24)$$

Each pixel is associated with the nearest cluster \mathbf{c}_n whose search area overlaps the pixel. After all pixels are associated with a cluster, a new cluster center is computed as the average vector of all the pixels belonging to the cluster. This is repeated for a set number of iterations. In the hyperspectral version of the SLIC algorithm, the option of relabelling disjoint segments is not performed, instead opting for higher selection of the m and n_s parameters to avoid disjoint segments all together. Once the algorithm is completed, the final superpixelated image is given by arranging the feature vectors into columns of the matrix $\mathbf{C} = [\mathbf{c}_1 \mid \mathbf{c}_2 \mid \dots \mid \mathbf{c}_{n_s}] \in \mathbb{R}^{n_\lambda \times n_s}$.

Algorithm 2: Hyperspectral SLIC Algorithm

Input:

Preprocessed Hyperspectral Image $\hat{\mathbf{X}}$, $m > 0$, $n_s > 0$, k_{\max}

Initialize:

$\mathbf{c}_n = [c_1, c_2, \dots, c_{n_s}]$ where $n = 1, \dots, n_s$ by sampling pixels at regular grid intervals S . Perturb cluster centers to lowest gradient position in a 3×3 neighborhood according to (23).

For $k = 0$ to k_{\max} :

Assign best matching pixels from a $2S \times 2S$ neighborhood around clusters $\mathbf{c}_1, \mathbf{c}_2, \dots, \mathbf{c}_{n_s}$ according to (24).

Compute new cluster centers according to average of all pixels belonging to cluster.

Output: Superpixelated Image Matrix \mathbf{C}

In the hyperspectral domain, superpixels are slightly less adept at creating visually meaningful partitioning due to use of the raw hyperspectral spectra rather than a perceptual color space like CIELAB. To alleviate this, higher values of m and n_s are used to form more spatially compact regions akin to the ones formed in the original algorithm. Nonetheless, superpixels are valuable in allowing practitioners to avoid having to consider the variation between individual pixels and instead consider the spectral and spatial variations between these new perceptual groupings of pixels.

3.3 Spatial Spectral Clustering

In Section 2.5, the Normalized Cuts algorithm was introduced for the task of bipartitioning a group of pixels through creating an affinity matrix and solving the relaxed eigensystem in (21). Considering a matrix of superpixels \mathbf{C} from the results of the SLIC algorithm in Section 3.2, two matrices are formed. The first matrix is the spectral affinity matrix $\mathbf{W}_{\text{spectral}}$ given by calculating the spectral angle between the spectral features of each pair of superpixels:

$$\mathbf{W}_{\text{spectral}(i,j)} = \arccos \left(\frac{\mathbf{c}_i \mathbf{c}_j^T}{\|\mathbf{c}_i\|_2 \|\mathbf{c}_j\|_2} \right) \quad (25)$$

The second matrix is the spatial distance matrix $\mathbf{W}_{\text{spatial}}$ given by calculating the spatial euclidean distance between each pair of superpixels:

$$\mathbf{W}_{\text{spatial}(i,j)} = d_{\text{spatial}}(\mathbf{c}_i, \mathbf{c}_j) \quad (26)$$

To combine the spatial and spectral information within the image, a spectral similarity parameter $\sigma > 0$ and spatial limit parameter $\kappa > 0$ are introduced and the spatial-spectral affinity matrix \mathbf{W} is then constructed as follows

$$\mathbf{W}_{(i,j)} = \begin{cases} \exp \left(-\frac{\mathbf{W}_{\text{spectral}(i,j)}^2}{\sigma^2} \right) & \text{if } \mathbf{W}_{\text{spatial}(i,j)} \leq \kappa \\ 0 & \text{if } \mathbf{W}_{\text{spatial}(i,j)} > \kappa \end{cases} \quad (27)$$

The intuition behind constructing the spatial-spectral affinity matrix is to calculate spectral similarity between two superpixels if and only if the centroids of the superpixels are within a spatial range κ of each other. This introduces spatial compactness within the partitioning.

After constructing the spatial-spectral affinity matrix, the goal is to then utilize the normalized cuts algorithm to recursively bi-partition the graph $G_{\mathbf{W}}$ represented by \mathbf{W} into n_e subgraphs. Doing so provides a segmentation of the columns of \mathbf{C} representing the superpixels into n_e clusters. Using the spatial-spectral affinity matrix \mathbf{W} , the diagonal matrix \mathbf{D} is calculated according (16) and the initial bi-partitioning of $G_{\mathbf{W}}$ can be determined by solving for the second smallest eigenvalue λ_2 and the corresponding eigenvector \mathbf{u}_2 in the system given in (21). Bi-partitioning the graph $G_{\mathbf{W}}$ according the sign of the entries in \mathbf{u}_2 , the next partition is given by the one that minimizes (19) within the two subgraphs. This process is continued until the graph $G_{\mathbf{W}}$ is partitioned into n_e subgraphs. Cluster membership of the superpixels in \mathbf{C} are assigned to the corresponding subgraph they belong to. Additionally, the mean spectral signatures of the superpixels within each cluster are calculated and arranged into the matrix \mathbf{M} .

Algorithm 3: Spatial Spectral Segmentation

Input: Superpixel Matrix \mathbf{C} , $\kappa > 0$, $\sigma > 0$, $n_e \geq 2$.

Initialize: Construct the spatial-spectral affinity matrix \mathbf{W} and diagonal matrix \mathbf{D} according to (27) and (16).

Recursion:

For each subgraph, solve the system (21). Bipartition the subgraph by assigning partition membership according to the cut that minimizes (19).

Output: Assign superpixel cluster memberships to a vector $\mathbf{v}_i \in \{1, 2, \dots, n_e\}$ according to the subgraph each node belongs to. Form an endmember spectra matrix $\mathbf{M} = [\mathbf{m}_1 | \mathbf{m}_2 | \dots | \mathbf{m}_{n_e}]$ where \mathbf{m}_i is the average spectral feature vector for all superpixels within the cluster i .

The algorithm allows for a flexible and efficient framework for segmentation tasks. The initial construction of the affinity matrix according to (27) needs to only be done once, with subsequent subsegmentations being done using selected columns and rows corresponding to the subgraphs each node belongs to. The most obvious bottleneck in the algorithm is the step in which the eigensystem is solved, scaling cubically with the number of superpixels n_s . The lower the number of superpixels, the faster the algorithm performs. On the other end, the higher the number of superpixels, the slower the algorithm performs. The final result is determined by tuning σ and κ . The lower σ is, the more of an emphasis the spectral features have on the final result, while, the lower κ is, the more of an emphasis the spatial information has on the final result. Careful selection of the two parameters allows for meaningful results.

3.4 Graph Regularized Abundance Estimation

In Section 2.3.2, the abundance estimation problem for a collection of pixels \mathbf{X} given the endmember spectra matrix \mathbf{M} was known was stated as follows:

$$\mathbf{A} = \arg \min_{\mathbf{A} \in \mathbb{R}^{n_e \times n_s}} \frac{1}{2} \|\mathbf{MA} - \mathbf{X}\|_F^2 + \chi_\Delta(\mathbf{A}) + J(\mathbf{A})$$

The goal of this section is to apply a similar framework to the collection of superpixels \mathbf{C} and determine estimates on the fractional abundances given an cluster spectra matrix \mathbf{M} from the output of the clustering in Section 3.3. The abundance estimation problem in terms of superpixels can now be restated as

$$\mathbf{A} = \arg \min_{\mathbf{A} \in \mathbb{R}^{n_e \times n_s}} \frac{1}{2} \|\mathbf{MA} - \mathbf{C}\|_F^2 + \chi_\Delta(\mathbf{A}) + J(\mathbf{A})$$

In previous sections, a regularization term J was introduced to provide further control on the final values of \mathbf{A} . In imaging applications, a common assumption is that color values should typically not vary greatly for pixels next to each other. In a similar fashion, abundance values should not vary greatly for superpixels spatially close to each other (Chen et al., 2023). To accommodate this assumption, the matrix $\mathbf{W}_{\text{spatial}}$ given in (26) can be exploited by considering

$$\mathbf{W}_{\kappa(i,j)} = \begin{cases} 1 & \text{if } \mathbf{W}_{\text{spatial}(i,j)} \leq \kappa \\ 0 & \text{if } \mathbf{W}_{\text{spatial}(i,j)} > \kappa \end{cases} \quad (28)$$

The regularization term

$$J(\mathbf{A}) = \frac{1}{2} \sum_{i=1}^{n_s} \sum_{j=1}^{n_s} \mathbf{W}_{\kappa(i,j)} \|\mathbf{a}_i - \mathbf{a}_j\|_2^2$$

is minimized under the assumption that \mathbf{a}_i and \mathbf{a}_j should be similar if \mathbf{c}_i and \mathbf{c}_j are spatially within a distance κ of each other. Importantly, J is convex and differentiable and can alternatively be represented using the corresponding Laplacian matrix \mathbf{L} described in (17) for the matrix \mathbf{W}_κ :

$$J(\mathbf{A}) = \frac{1}{2} \sum_{i=1}^{n_s} \sum_{j=1}^{n_s} \mathbf{W}_{\kappa(i,j)} \|\mathbf{a}_i - \mathbf{a}_j\|_2^2 = \text{tr}(\mathbf{ALA}^T) \quad (29)$$

The graph regularized abundance estimation problem with the known cluster spectra matrix \mathbf{M} and regularization weight parameter $\beta > 0$ is represented as:

$$\mathbf{A} = \arg \min_{\mathbf{A} \in \mathbb{R}^{n_e \times n_s}} \frac{1}{2} \|\mathbf{MA} - \mathbf{C}\|_F^2 + \chi_\Delta(\mathbf{A}) + \frac{\beta}{2} \text{tr}(\mathbf{ALA}^T) \quad (30)$$

The goal of this rest of the section is to demonstrate how this problem can be equivalently represented in a form where the Alternating Direction Method of Multipliers technique can be applied. The abundance estimation problem when one or more than one regularization terms are added belongs to a class of problems called global consensus optimization problems shown in (Boyd et al., 2011). The standard approach to transforming (30) is to introduce matrices $\mathbf{U} \in \mathbb{R}^{n_e \times n_s}$, $\mathbf{V}_1 \in \mathbb{R}^{n_b \times n_s}$, $\mathbf{V}_2 \in \mathbb{R}^{n_e \times n_s}$, and $\mathbf{V}_3 \in \mathbb{R}^{n_e \times n_s}$ and rewrite the problem as:

$$\begin{aligned} & \underset{\mathbf{U}, \mathbf{V}_1, \mathbf{V}_2, \mathbf{V}_3}{\text{minimize}} && \frac{1}{2} \|\mathbf{V}_1 - \mathbf{C}\|_F^2 + \chi_\Delta(\mathbf{V}_2) + \frac{\beta}{2} \text{tr}(\mathbf{V}_3 \mathbf{L} \mathbf{V}_3^T) \\ & \text{subject to} && \mathbf{V}_1 = \mathbf{M} \mathbf{U} \\ & && \mathbf{V}_2 = \mathbf{U} \\ & && \mathbf{V}_3 = \mathbf{U} \end{aligned} \quad (31)$$

Further manipulation shows that by letting $g(\mathbf{V}) = \frac{1}{2} \|\mathbf{V}_1 - \mathbf{C}\|_F^2 + \chi_\Delta(\mathbf{V}_2) + \frac{\beta}{2} \text{tr}(\mathbf{V}_3 \mathbf{L} \mathbf{V}_3^T)$,

$$\mathbf{V} = \begin{bmatrix} \mathbf{V}_1 & & \\ & \mathbf{V}_2 & \\ & & \mathbf{V}_3 \end{bmatrix}, \quad \mathbf{G} = \begin{bmatrix} \mathbf{M} \\ \mathbf{I} \\ \mathbf{I} \end{bmatrix}, \quad \mathbf{B} = \begin{bmatrix} -\mathbf{I} & & \\ & -\mathbf{I} & \\ & & -\mathbf{I} \end{bmatrix}$$

The problem in (31) can then be rewritten in an equivalent form as

$$\begin{aligned} & \underset{\mathbf{U}, \mathbf{V}}{\text{minimize}} && g(\mathbf{V}) \\ & \text{subject to} && \mathbf{G} \mathbf{U} + \mathbf{B} \mathbf{V} = \mathbf{0} \end{aligned} \quad (32)$$

The scaled augmented lagrangian \mathcal{L}_μ with parameter $\mu > 0$ and scaled dual variable \mathbf{D} is then given as:

$$\mathcal{L}_\mu(\mathbf{U}, \mathbf{V}, \mathbf{D}) = g(\mathbf{V}) + \frac{\mu}{2} \|\mathbf{G} \mathbf{U} + \mathbf{B} \mathbf{V} - \mathbf{D}\|_F^2 \quad (33)$$

where

$$\mathbf{D} = \begin{bmatrix} \mathbf{D}_1 & & \\ & \mathbf{D}_2 & \\ & & \mathbf{D}_3 \end{bmatrix}$$

ADMM aims to minimize scaled form of \mathcal{L}_μ by alternating minimizations with respect to \mathbf{U} , \mathbf{V} , and \mathbf{D} by performing the following updates:

$$\begin{aligned} \mathbf{U}^{(k+1)} &= \arg \min_{\mathbf{U}} \frac{\mu}{2} \|\mathbf{G} \mathbf{U} + \mathbf{B} \mathbf{V}^{(k)} - \mathbf{D}^{(k)}\|_F^2 \\ \mathbf{V}^{(k+1)} &= \arg \min_{\mathbf{V}} g(\mathbf{V}) + \frac{\mu}{2} \|\mathbf{G} \mathbf{U}^{(k+1)} + \mathbf{B} \mathbf{V} - \mathbf{D}^{(k)}\|_F^2 \\ \mathbf{D}^{(k+1)} &= \mathbf{D}^{(k)} - \mathbf{G} \mathbf{U}^{(k+1)} - \mathbf{B} \mathbf{V}^{(k+1)} \end{aligned} \quad (34)$$

While the updates are in a simpler format, further work needs to be done to derive updates for \mathbf{V} . Looking at the $\|\mathbf{G} \mathbf{U} + \mathbf{B} \mathbf{V}^{(k)} - \mathbf{D}^{(k)}\|_F^2$ term in (33), the structure of it's components give leeway to splitting the term into individual components, notably

$$\begin{aligned} \|\mathbf{G} \mathbf{U} + \mathbf{B} \mathbf{V} - \mathbf{D}\|_F^2 &= \left\| \begin{bmatrix} \mathbf{M} \mathbf{U} - \mathbf{V}_1 - \mathbf{D}_1 & & \\ & \mathbf{U} - \mathbf{V}_2 - \mathbf{D}_2 & \\ & & \mathbf{U} - \mathbf{V}_3 - \mathbf{D}_3 \end{bmatrix} \right\|_F^2 \\ &= \|\mathbf{M} \mathbf{U} - \mathbf{V}_1 - \mathbf{D}_1\|_F^2 + \|\mathbf{U} - \mathbf{V}_2 - \mathbf{D}_2\|_F^2 + \|\mathbf{U} - \mathbf{V}_3 - \mathbf{D}_3\|_F^2 \end{aligned}$$

Applying this expansion, the updates in (34) can be rewritten. The \mathbf{U} update becomes

$$\begin{aligned} \mathbf{U}^{(k+1)} &= \arg \min_{\mathbf{U}} \frac{\mu}{2} \|\mathbf{M} \mathbf{U} - \mathbf{V}_1^{(k)} - \mathbf{D}_1^{(k)}\|_F^2 \\ &\quad + \frac{\mu}{2} \|\mathbf{U} - \mathbf{V}_2^{(k)} - \mathbf{D}_2^{(k)}\|_F^2 \\ &\quad + \frac{\mu}{2} \|\mathbf{U} - \mathbf{V}_3^{(k)} - \mathbf{D}_3^{(k)}\|_F^2 \end{aligned} \quad (35)$$

Under the same expansion, the \mathbf{V} update becomes

$$\begin{aligned}\mathbf{V}^{(k+1)} = \arg \min_{\mathbf{V}} & \frac{1}{2} \|\mathbf{V}_1 - \mathbf{C}\|_F^2 + \chi_{\Delta}(\mathbf{V}_2) + \frac{\beta}{2} \text{tr}(\mathbf{V}_3 \mathbf{L} \mathbf{V}_3^T) \\ & + \frac{\mu}{2} \|\mathbf{M} \mathbf{U}^{(k+1)} - \mathbf{V}_1 - \mathbf{D}_1^{(k)}\|_F^2 \\ & + \frac{\mu}{2} \|\mathbf{U}^{(k+1)} - \mathbf{V}_2 - \mathbf{D}_2^{(k)}\|_F^2 \\ & + \frac{\mu}{2} \|\mathbf{U}^{(k+1)} - \mathbf{V}_3 - \mathbf{D}_3^{(k)}\|_F^2\end{aligned}$$

Furthermore, each component of the update for \mathbf{V} can be split into individual updates for \mathbf{V}_1 , \mathbf{V}_2 and \mathbf{V}_3 ,

$$\begin{aligned}\mathbf{V}_1^{(k+1)} &= \arg \min_{\mathbf{V}_1} \frac{1}{2} \|\mathbf{V}_1 - \mathbf{C}\|_F^2 + \frac{\mu}{2} \|\mathbf{M} \mathbf{U}^{(k+1)} - \mathbf{V}_1 - \mathbf{D}_1^{(k)}\|_F^2 \\ \mathbf{V}_2^{(k+1)} &= \arg \min_{\mathbf{V}_2} \chi_{\Delta}(\mathbf{V}_2) + \frac{\mu}{2} \|\mathbf{U}^{(k+1)} - \mathbf{V}_2 - \mathbf{D}_2^{(k)}\|_F^2 \\ \mathbf{V}_3^{(k+1)} &= \arg \min_{\mathbf{V}_3} \frac{\beta}{2} \text{tr}(\mathbf{V}_3 \mathbf{L} \mathbf{V}_3^T) + \frac{\mu}{2} \|\mathbf{U}^{(k+1)} - \mathbf{V}_3 - \mathbf{D}_3^{(k)}\|_F^2\end{aligned}\tag{36}$$

Lastly, in similar fashion to \mathbf{V} , the \mathbf{D} update in (34) can also be split component wise:

$$\begin{aligned}\mathbf{D}_1^{(k+1)} &= \mathbf{D}_1^{(k)} - \mathbf{M} \mathbf{U}^{(k+1)} + \mathbf{V}_1^{(k+1)} \\ \mathbf{D}_2^{(k+1)} &= \mathbf{D}_2^{(k)} - \mathbf{U}^{(k+1)} + \mathbf{V}_2^{(k+1)} \\ \mathbf{D}_3^{(k+1)} &= \mathbf{D}_3^{(k)} - \mathbf{U}^{(k+1)} + \mathbf{V}_3^{(k+1)}\end{aligned}\tag{37}$$

Taking into account (35), (36), (37), the updates in (34) can finally be rewritten in the expanded form as:

$$\begin{aligned}\mathbf{U}^{(k+1)} &= \arg \min_{\mathbf{U}} \frac{\mu}{2} \|\mathbf{M} \mathbf{U} - \mathbf{V}_1^{(k)} - \mathbf{D}_1^{(k)}\|_F^2 + \frac{\mu}{2} \|\mathbf{U} - \mathbf{V}_2^{(k)} - \mathbf{D}_2^{(k)}\|_F^2 + \frac{\mu}{2} \|\mathbf{U} - \mathbf{V}_3^{(k)} - \mathbf{D}_3^{(k)}\|_F^2 \\ \mathbf{V}_1^{(k+1)} &= \arg \min_{\mathbf{V}_1} \frac{1}{2} \|\mathbf{V}_1 - \mathbf{C}\|_F^2 + \frac{\mu}{2} \|\mathbf{M} \mathbf{U}^{(k+1)} - \mathbf{V}_1 - \mathbf{D}_1^{(k)}\|_F^2 \\ \mathbf{V}_2^{(k+1)} &= \arg \min_{\mathbf{V}_2} \chi_{\Delta}(\mathbf{V}_2) + \frac{\mu}{2} \|\mathbf{U}^{(k+1)} - \mathbf{V}_2 - \mathbf{D}_2^{(k)}\|_F^2 \\ \mathbf{V}_3^{(k+1)} &= \arg \min_{\mathbf{V}_3} \frac{\beta}{2} \text{tr}(\mathbf{V}_3 \mathbf{L} \mathbf{V}_3^T) + \frac{\mu}{2} \|\mathbf{U}^{(k+1)} - \mathbf{V}_3 - \mathbf{D}_3^{(k)}\|_F^2 \\ \mathbf{D}_1^{(k+1)} &= \mathbf{D}_1^{(k)} - \mathbf{M} \mathbf{U}^{(k+1)} + \mathbf{V}_1^{(k+1)} \\ \mathbf{D}_2^{(k+1)} &= \mathbf{D}_2^{(k)} - \mathbf{U}^{(k+1)} + \mathbf{V}_2^{(k+1)} \\ \mathbf{D}_3^{(k+1)} &= \mathbf{D}_3^{(k)} - \mathbf{U}^{(k+1)} + \mathbf{V}_3^{(k+1)}\end{aligned}\tag{38}$$

The updates for \mathbf{U} and \mathbf{V}_1 have closed form solutions due to convexity and differentiability of the Frobenius norm. Both updates can be derived by taking the partial derivatives with respect to the individual terms, setting them equal to $\mathbf{0}$, and solving accordingly. For the \mathbf{U} update,

$$\begin{aligned}\mathbf{0} &= \frac{\partial}{\partial \mathbf{U}} \left[\frac{\mu}{2} \|\mathbf{M} \mathbf{U} - \mathbf{V}_1 - \mathbf{D}_1\|_F^2 + \frac{\mu}{2} \|\mathbf{U} - \mathbf{V}_2 - \mathbf{D}_2\|_F^2 + \frac{\mu}{2} \|\mathbf{U} - \mathbf{V}_3 - \mathbf{D}_3\|_F^2 \right] \\ \mathbf{0} &= \mu (\mathbf{M}^T (\mathbf{M} \mathbf{U} - \mathbf{V}_1 - \mathbf{D}_1) + (\mathbf{U} - \mathbf{V}_2 - \mathbf{D}_2) + (\mathbf{U} - \mathbf{V}_3 - \mathbf{D}_3)) \\ \mathbf{M}^T \mathbf{M} \mathbf{U} + 2\mathbf{U} &= \mathbf{M}^T (\mathbf{V}_1 + \mathbf{D}_1) + (\mathbf{V}_2 + \mathbf{D}_2) + (\mathbf{V}_3 + \mathbf{D}_3) \\ \mathbf{U} &= (\mathbf{M}^T \mathbf{M} + 2\mathbf{I})^{-1} (\mathbf{M}^T (\mathbf{V}_1 + \mathbf{D}_1) + (\mathbf{V}_2 + \mathbf{D}_2) + (\mathbf{V}_3 + \mathbf{D}_3))\end{aligned}$$

As \mathbf{M} is known and unchanged, $(\mathbf{M}^T \mathbf{M} + 2\mathbf{I})^{-1}$ can be calculated and cached once for the entire runtime. For the \mathbf{V}_1 update,

$$\begin{aligned}\mathbf{0} &= \frac{\partial}{\partial \mathbf{V}_1} \left[\frac{1}{2} \|\mathbf{V}_1 - \mathbf{C}\|_F^2 + \frac{\mu}{2} \|\mathbf{M} \mathbf{U} - \mathbf{V}_1 - \mathbf{D}_1\|_F^2 \right] \\ \mathbf{0} &= (\mathbf{V}_1 - \mathbf{C}) + \mu (\mathbf{V}_1 - (\mathbf{M} \mathbf{U} - \mathbf{D}_1)) \\ \mathbf{V}_1 &= \frac{1}{1 + \mu} (\mathbf{C} + (\mathbf{M} \mathbf{U} - \mathbf{D}_1))\end{aligned}$$

While the update for \mathbf{V}_2 does not have a closed form solution, it is important to note that the update \mathbf{V}_2 can be equivalently rewritten as:

$$\mathbf{V}_2^{(k+1)} = \arg \min_{\mathbf{V}_2 \in \Delta} \frac{\mu}{2} \|\mathbf{U}^{(k+1)} - \mathbf{V}_2 - \mathbf{D}_2^{(k)}\|_F^2$$

The update, in non-formulaic terms, requires finding \mathbf{V}_2 that minimizes $\frac{\mu}{2} \|\mathbf{U}^{(k+1)} - \mathbf{V}_2 - \mathbf{D}_2^{(k)}\|_F^2$, then projecting the solution onto Δ . The non-projected minimum can be found in the same way as the updates for \mathbf{V} and \mathbf{U}

$$\begin{aligned} \mathbf{0} &= \frac{\partial}{\partial \mathbf{V}_2} \left[\frac{\mu}{2} \|\mathbf{U} - \mathbf{V}_2 - \mathbf{D}_2\|_F^2 \right] \\ \mathbf{0} &= \mu(\mathbf{V}_2 - (\mathbf{M}\mathbf{U} - \mathbf{D}_2)) \\ \mathbf{V}_2 &= \mathbf{M}\mathbf{U} - \mathbf{D}_2 \end{aligned}$$

The orthogonal projection of a matrix \mathbf{C} onto the convex and closed set Δ is defined as the finding the matrix $\tilde{\mathbf{C}} \in \Delta$ that minimizes the least-squares error between the two matrices. Multiple numerical methods exist for computing the projection (Condat, 2016). Formally, the projection can simply be written as follows.

$$\text{proj}_\Delta(\mathbf{C}) = \arg \min_{\tilde{\mathbf{C}} \in \Delta} \|\tilde{\mathbf{C}} - \mathbf{C}\|_F^2$$

Thus, applying the projection, the update for \mathbf{V}_2 is given as

$$\mathbf{V}_2 = \text{proj}_\Delta(\mathbf{M}\mathbf{U} - \mathbf{D}_2)$$

The approach for deriving update for \mathbf{V}_3 follows the same as \mathbf{U} and \mathbf{V}_1 due to the convexity and differentiability of the regularization term $\text{tr}(\mathbf{V}_3 \mathbf{L} \mathbf{V}_3^T)$.

$$\begin{aligned} \mathbf{0} &= \frac{\partial}{\partial \mathbf{V}_3} \left[\frac{\beta}{2} \text{tr}(\mathbf{V}_3 \mathbf{L} \mathbf{V}_3^T) + \frac{\mu}{2} \|\mathbf{U} - \mathbf{V}_3 - \mathbf{D}_3\|_F^2 \right] \\ \mathbf{0} &= \frac{\beta}{2} (\mathbf{V}_3 \mathbf{L}^T + \mathbf{V}_3 \mathbf{L}) + \mu(\mathbf{V}_3 - (\mathbf{U} - \mathbf{D}_3)) \\ \mathbf{0} &= \beta \mathbf{V}_3 \mathbf{L} + \mu \mathbf{V}_3 - \mu(\mathbf{U} - \mathbf{D}_3) \\ \mathbf{V}_3 \left(\mathbf{L} + \frac{\mu}{\beta} \mathbf{I} \right) &= \frac{\mu}{\beta} (\mathbf{U} - \mathbf{D}_3) \\ \mathbf{V}_3 &= \frac{\mu}{\beta} (\mathbf{U} - \mathbf{D}_3) \left(\mathbf{L} + \frac{\mu}{\beta} \mathbf{I} \right)^{-1} \end{aligned}$$

As \mathbf{L} is a real valued, symmetric matrix, it can be eigendecomposed into the product $\mathbf{L} = \mathbf{S} \mathbf{\Sigma} \mathbf{S}^T$, where \mathbf{S} is a matrix whose columns are the eigenvectors of \mathbf{L} , and $\mathbf{\Sigma}$ is a matrix whose diagonal elements are the eigenvalues of \mathbf{L} . Additionally, \mathbf{S} is an orthogonal matrix, as such, $\mathbf{S}^T = \mathbf{S}^{-1}$ and $\mathbf{S} \mathbf{S}^T = \mathbf{I}$. One important note to be made about the update step is that computing the inverse of the term $(\mathbf{L} + \mu/\beta \mathbf{I})$ is slower than computing the eigendecomposition \mathbf{L} due to the naturally sparse definition of \mathbf{L} and it's underlying distance matrix \mathbf{W}_κ . Using that information, a more efficient update can be performed by calculating the eigendecomposition $\mathbf{L} = \mathbf{S} \mathbf{\Sigma} \mathbf{S}^T$ and simplifying the update for \mathbf{V}_3 as follows:

$$\begin{aligned} \mathbf{V}_3 &= \frac{\mu}{\beta} (\mathbf{U} - \mathbf{D}_3) \left(\mathbf{L} + \frac{\mu}{\beta} \mathbf{I} \right)^{-1} \\ \mathbf{V}_3 &= \frac{\mu}{\beta} (\mathbf{U} - \mathbf{D}_3) \left(\mathbf{S} \mathbf{\Sigma} \mathbf{S}^T + \frac{\mu}{\beta} \mathbf{S} \mathbf{S}^T \right)^{-1} \\ \mathbf{V}_3 &= \frac{\mu}{\beta} (\mathbf{U} - \mathbf{D}_3) \left(\mathbf{S} \left(\mathbf{\Sigma} + \frac{\mu}{\beta} \mathbf{I} \right) \mathbf{S}^T \right)^{-1} \\ \mathbf{V}_3 &= \frac{\mu}{\beta} (\mathbf{U} - \mathbf{D}_3) \mathbf{S} \left(\mathbf{\Sigma} + \frac{\mu}{\beta} \mathbf{I} \right)^{-1} \mathbf{S}^T \end{aligned}$$

The values along the diagonal in $\mathbf{\Sigma}$ are all non negative due to \mathbf{L} having non negative eigenvalues. As such, the matrix $(\mathbf{\Sigma} + \mu/\beta \mathbf{I})$ is a diagonal matrix with it's elements being all strictly positive. The inverse of $(\mathbf{\Sigma} + \mu/\beta \mathbf{I})$ can be directly calculated as by taking the reciprocal of it's diagonal elements. As \mathbf{L} is known at the onset of the

algorithm and the parameters μ and β do not change between iterations, $\mathbf{S}(\mathbf{\Sigma} + \mu/\beta\mathbf{I})^{-1}\mathbf{S}^T$ can be cached and reused across iterations.

The derived updates in (38), for parameters $\mu > 0$ and $\beta > 0$ are subsequently given as:

$$\mathbf{U}^{(k+1)} = (\mathbf{M}^T\mathbf{M} + 2\mathbf{I})^{-1} \left(\mathbf{M}^T \left(\mathbf{V}_1^{(k)} + \mathbf{D}_1^{(k)} \right) + \left(\mathbf{V}_2^{(k)} + \mathbf{D}_2^{(k)} \right) + \left(\mathbf{V}_3^{(k)} + \mathbf{D}_3^{(k)} \right) \right) \quad (39a)$$

$$\mathbf{V}_1^{(k+1)} = \frac{1}{1+\mu} \left(\mathbf{C} + \left(\mathbf{M}\mathbf{U}^{(k+1)} - \mathbf{D}_1^{(k)} \right) \right) \quad (39b)$$

$$\mathbf{V}_2^{(k+1)} = \text{proj}_{\Delta} \left(\mathbf{M}\mathbf{U}^{(k+1)} - \mathbf{D}_2^{(k)} \right) \quad (39c)$$

$$\mathbf{V}_3^{(k+1)} = \frac{\mu}{\beta} \left(\mathbf{U}^{(k+1)} - \mathbf{D}_3^{(k)} \right) \mathbf{S} \left(\mathbf{\Sigma} + \frac{\mu}{\beta}\mathbf{I} \right)^{-1} \mathbf{S}^T \quad (39d)$$

$$\mathbf{D}_1^{(k+1)} = \mathbf{D}_1^{(k)} - \mathbf{M}\mathbf{U}^{(k+1)} + \mathbf{V}_1^{(k+1)} \quad (39e)$$

$$\mathbf{D}_2^{(k+1)} = \mathbf{D}_2^{(k)} - \mathbf{U}^{(k+1)} + \mathbf{V}_2^{(k+1)} \quad (39f)$$

$$\mathbf{D}_3^{(k+1)} = \mathbf{D}_3^{(k)} - \mathbf{U}^{(k+1)} + \mathbf{V}_3^{(k+1)} \quad (39g)$$

The algorithm is set to terminate when $\|\mathbf{U}^{(k+1)} - \mathbf{U}^{(k)}\|_F / \|\mathbf{U}^{(k)}\|_F$ falls below a set tolerance ϵ or the algorithm reaches a maximum iterative index of k_{\max} . After such point, $\mathbf{U}^{(k+1)}$ is given as the final result, representing the approximate solution of \mathbf{A} to the minimization problem described in (30). In its entirety, the abundance estimation algorithm can be described with the following algorithm outline.

Algorithm 4: Graph Regularized Abundance Estimation

Input:

$\mathbf{C}, \mathbf{M}, \mathbf{W}_{\kappa}, \beta > 0, \mu > 0, k_{\max} > 0, \epsilon > 0.$

Initialize:

Precompute and cache $\mathbf{S}(\mathbf{\Sigma} + \mu/\beta\mathbf{I})^{-1}\mathbf{S}^T$ and $(\mathbf{M}^T\mathbf{M} + 2\mathbf{I})^{-1}$

$\mathbf{U}^{(0)} \in \Delta$

$\mathbf{V}_1^{(0)} = \mathbf{M}\mathbf{U}^{(0)}$

$\mathbf{V}_2^{(0)} = \mathbf{U}^{(0)}$

$\mathbf{V}_3^{(0)} = \mathbf{U}^{(0)}$

$\mathbf{D}_1^{(0)} = \mathbf{0}$

$\mathbf{D}_2^{(0)} = \mathbf{0}$

$\mathbf{D}_3^{(0)} = \mathbf{0}$

For $k = 0$ to k_{\max} :

Update $\mathbf{U}^{(k+1)}$ according to (39a)

Update $\mathbf{V}_1^{(k+1)}$ according to (39b)

Update $\mathbf{V}_2^{(k+1)}$ according to (39c)

Update $\mathbf{V}_3^{(k+1)}$ according to (39d)

Update $\mathbf{D}_1^{(k+1)}$ according to (39e)

Update $\mathbf{D}_2^{(k+1)}$ according to (39f)

Update $\mathbf{D}_3^{(k+1)}$ according to (39g)

Break if $\|\mathbf{U}^{(k+1)} - \mathbf{U}^{(k)}\|_F / \|\mathbf{U}^{(k)}\|_F < \epsilon$

Output:

Abundance Matrix $\mathbf{A} = \mathbf{U}$

The ADMM-variant of the abundance estimation algorithm described above gives a efficient solution to in a relatively low number of iterations. Additional inquiry shows that the updates for \mathbf{V} and \mathbf{D} can be done completely in parallel, allowing for further performance optimization. In practical applications, β is the only parameter to be tuned, corresponding to the strength of the spatial regularization, κ is predefined in Section 3.3, as such it is not the focus of tuning in this step.

3.5 Feature Vector Creation

The abundance estimation problem described in Section 3.4 outputs a matrix $\mathbf{A} \in \mathbb{R}_+^{n_e \times n_p}$ whose columns \mathbf{a}_i hold the abundance values for the superpixel \mathbf{c}_i with respect to the mean spectral signatures. The initial partitioning of the set of superpixels performed in Section 3.3 often provides an adequate solution, however, there is always hope

to further refine the segmentation (Al-Khafaji et al., 2022). In the effort to do so, a new superpixel feature vector is created by concatenating the original spectral features and the abundance estimation results

$$\tilde{\mathbf{c}}_i = \mathbf{c}_i \oplus \mathbf{a}_i \quad (40)$$

With the new construction of $\tilde{\mathbf{c}}$, the segmentation described in Section 3.3 is repeated with the same set of parameters σ and κ . The overall intuition behind this final step is to combine these additional, rich abundance features and the original spectral information to produce a more accurate segmentation. This proves useful along the boundaries between regions, where the creation of superpixels leads to mixed pixels. The added abundance information aids in adequately segmenting these mixed regions. The further refinement through the inclusion of the abundance information allows stronger spatial coherence in the clusters, due to the use of the graph regularization in (30).

3.6 Algorithm Overview

In summary, the algorithm can be described as follows

Algorithm 5: Adaptive Superpixel Cuts for Hyperspectral Images

Input:

Hyperspectral Image $\mathbf{X} \in \mathbb{R}_+^{n_x \times n_y \times n_\lambda}$.
 Superpixel Parameters: n_s, m
 Segmentation Parameters: n_e, σ, κ
 Abundance Estimation Parameters: μ, β

Preprocessing:

Create Normalized Hyperspectral Image $\hat{\mathbf{X}}$ according to (22).

Superpixel Creation:

Generate superpixel matrix $\mathbf{C} \in \mathbb{R}_+^{n_\lambda \times n_s}$ according to Algorithm 2 with parameters n_s, m .

Spatial Spectral Segmentation:

Perform an initial segmentation of the columns of the superpixel matrix \mathbf{C} into n_e partitions and form the spectra matrix $\mathbf{M} \in \mathbb{R}_+^{n_\lambda \times n_e}$ according to Algorithm 3 with parameters n_e, σ, κ .

Abundance Estimation:

Perform abundance estimation to the columns of the superpixel matrix \mathbf{C} relative to the spectra matrix \mathbf{M} , obtaining abundance matrix $\mathbf{A} \in \mathbb{R}_+^{n_e \times n_s}$ according to Algorithm 4 with parameters μ, β .

Feature Vector Creation

Form the feature matrix $\tilde{\mathbf{C}} \in \mathbb{R}_+^{(n_\lambda + n_e) \times n_s}$ according to (40)

Spatial Spectral Segmentation:

Perform the final segmentation of the columns of the superpixel matrix $\tilde{\mathbf{C}}$ into n_e partitions according to Algorithm 3 with parameters n_e, σ, κ .

Output:

Label vector \mathbf{v} , where $v_i \in 1, 2, \dots, n_e$, corresponding to the final segmentation of the superpixels.

The superpixel parameters n_s and m are one time selections based off the requirements of the practioners, as n_s determines the runtime of the algorithm. If n_s is set too high, the more the superpixels resemble the original image itself, giving zero benefit to using a superpixel approach. Careful and reasonable selection of n_s and m should be done based off the requirements of the specific analysis to be done. In practice, setting n_s such that $\frac{n_p}{n_s} \approx 16$ allows adequate results without extensive tuning of m . In similar fashion, the abundance estimation parameters μ and β are one time, global selections. As mentioned in Section 2.4, the ADMM method provides modest accuracy solutions in a relatively low number of operations. In practice, the results of the algorithm are largely insensitive to selection of μ . In a similar manner, β serves the purpose of reducing relative variations in abundance estimates between nearby superpixels, which aids in instances where two regions share similar spectral characteristics but are spatially distinct.

In application, the choice of parameters primarily focuses on on the segmentation parameters n_e, σ, κ as they dictate the initial and final segmentation of the image itself. Selection should be done to ensure an informative initial segmentation, then allow the algorithm to further refine it for the final segmentation according to the specific domain requirements.

4 Experimental Results

Having presented the details of the proposed approach, this section aims to document the experimental evaluation of its performance with respect to well studied hyperspectral datasets in the remote sensing field. Additionally, comparison in results is made to two popular segmentation algorithms. This section will demonstrate the ability of our method to achieve accurate segmentation, with a focus on its advantages in handling mixed pixels and spatially separated materials.

4.1 Evaluation Datasets

There exist two popular datasets in the remote sensing community are the Samson and Salinas dataset.

The Salinas is a 512-by-217 hyperspectral image collected by the 224-band AVIRIS sensor over Salinas Valley, California, and is characterized by high spatial resolution (3.7-meter pixels) with spectral wavelengths from 400 to 2500 nanometers. 20 spectral bands were removed from the image corresponding to high-noise channels, resulting in a total of 204 captured spectral bands. The image is comprised of 16 classifications based on various vegetation and vineyard types.

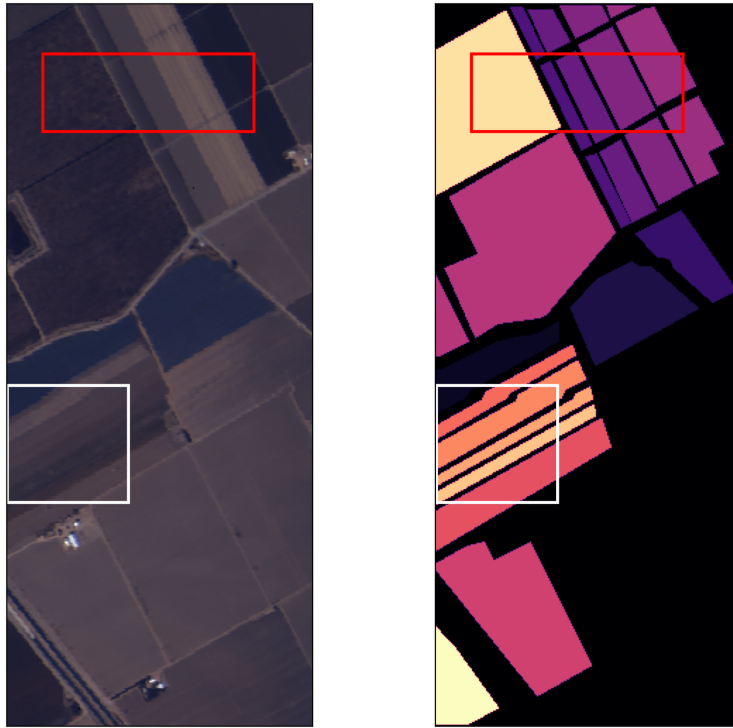


Figure 1: Colorized Salinas & Ground Truth Labels with Subsets A (White Box) & B (Red Box)

The Salinas dataset is commonly used in hyperspectral classification evaluation due to the availability of ground truth labels within the image. Due to similar spectral characteristics of multiple vegetation types in the image, this dataset is optimal to test the efficacy of the proposed algorithm in segmentation tasks. There are two subsets of the Salinas commonly used for evaluation. Salinas A is a 86-by-83 pixel subset of the Salinas image beginning from pixel index (270, 0) with 6 classifications. Salinas B is a 55-by-150 pixel subset of the Salinas image beginning from pixel index (35, 25) with 5 classifications. Both subsections provide an adequate mix of vegetation types.

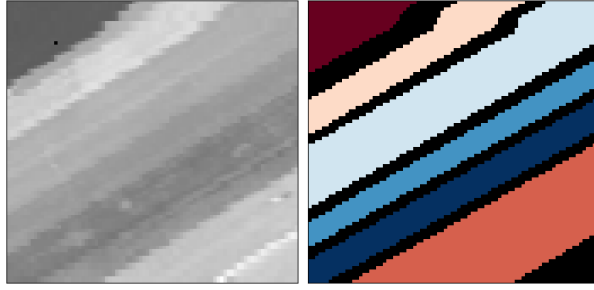


Figure 2: Greyscale Salinas-A & Ground Truth Labels

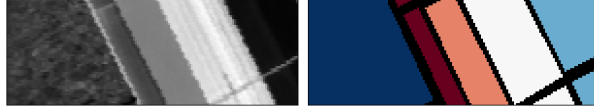


Figure 3: Greyscale Salinas-B & Ground Truth Labels

In similar fashion, Samson is a 952-by-952 hyperspectral image captured by 156-band SAMSON sensor over Elkhorn, California. The image covers a spectral range of 400nm to 900nm with a bandwidth of 3.2nm. This image does not include any ground truth labels, however subsets of the image are created comprised of soil, trees, and water.



Figure 4: Colorized Samson & with Subsets A (Red), B (Blue), C (Green)

The Samson-A, Samson-B, Samson-C subsets are all 95-by-95 hyperspectral images of regions originating from pixel indices (332, 252), (93, 232) and (345, 545) respectively. The subsets are comprised of the shore lines of where there are many mixed pixel measurements occur due the mixing of materials and complex forms created by the distribution of materials.

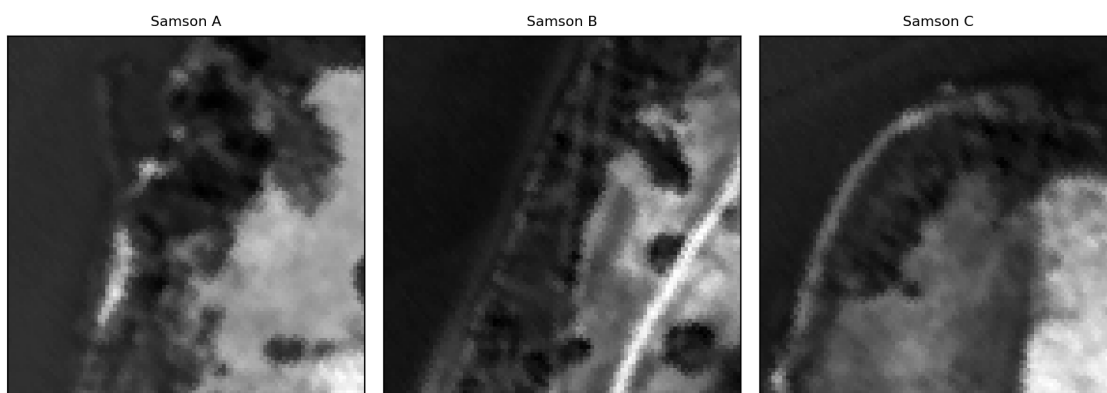


Figure 5: Greyscale Samson Subsets

4.2 Algorithm Evaluation

All experiments were performed on an 8-core AMD Ryzen 9 6900HS with 32GB of 4800MHz RAM. The implementation of the algorithm was done in Python 3.11 using the numpy and scipy libraries.

4.2.1 Quantitative Evaluation on Salinas

Our proposed segmentation algorithm was applied to the Salinas dataset and its performance was evaluated using established evaluation metrics like Overall Accuracy (OA), Average Segmentation Accuracy (ASA), and Intersection over Union (IoU) for individual classes. This evaluation will allow us to assess the effectiveness of our algorithm in segmenting the Salinas scene, particularly focusing on its ability to accurately identify and delineate the various material classes present within the dataset.

For Salinas-A, prior knowledge about the scene confirms the aim is to segment the image into $n_e = 6$ segments corresponding to the following vegetation classifications in the image. One important note is that Label 2 - Corn-senesced green weed is commonly understood to be incorrectly label, this is due to the presence of two differing spectral signatures in endmember. As such, the aim is to then segment the image in $n_e = 7$ segments corresponding to this new spectral distinction within Label 2. For the sake of evaluation against the known labels, segmentations created by the algorithm within this region will be joined into one label.

Label	Class	Samples
1	Broccoli green weeds 1	391
2	Corn-senesced green weeds	1343
3	Lettuce romaine 4wk	616
4	Lettuce romaine 5wk	1525
5	Lettuce romaine 6wk	674
6	Lettuce romaine 7wk	799

Table 1: Groundtruth classes for the Salinas-A scene and their respective samples number

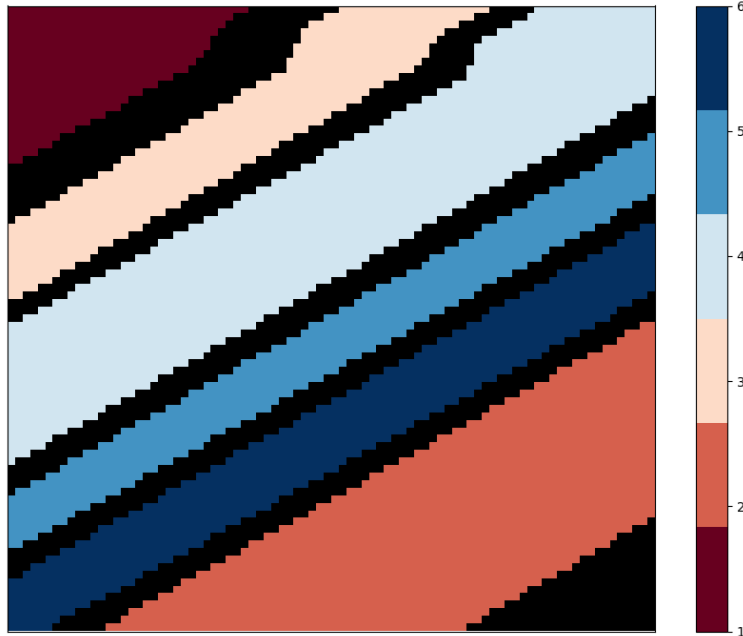


Figure 6: Salinas-A Ground Truth Labels

Using an initial selection of $n_s = 420$ superpixels with shape parameter $m = 2$ and unmixing parameters $\mu = 1$ and $\beta = 0.0025$, a grid search was applied to σ and κ such that $\sigma \in [0.1, 0.001]$ and $\kappa \in [15, 40]$, to which $\sigma = 0.0025$ and $\kappa = 20$ produced the most optimal results with an overall accuracy of 0.993.

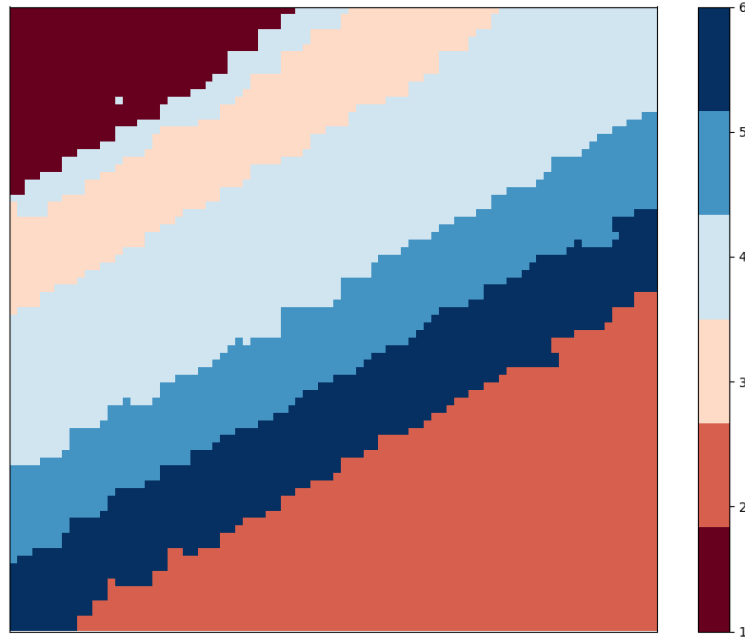


Figure 7: Salinas-A Algorithm Results

In the case of this specific segmentation, Label 2 is comprised of two individual segments were combined to match with the comparison to the original Corn-senesced green weed class. The algorithm itself performs well across all classes, with high individual segment accuracy scores as well as IoU scores, demonstrating it's ability to perform segmentation in scenarios where similar spectral features are shared among materials and materials span across the image.

	1	2	3	4	5	6	Accuracy	IoU
1	390	0	0	10	0	0	0.997	0.997
2	0	1343	0	0	0	0	1.000	0.987
3	0	0	598	180	0	0	0.971	0.971
4	0	0	0	1525	0	0	1.000	0.988
5	0	0	0	0	671	30	0.996	0.996
6	0	180	0	0	0	781	0.977	0.974

Table 2: Pixel-wise Confusion Matrix (Vertical: Actual, Horizontal: Predicted)

Salinas-B is a simpler segmentation case, prior knowledge about the scene confirms the aim is to segment the image into $n_e = 5$ segments corresponding to the following vegetation classifications in the image.

Label	Class	Samples
1	Fallow Rough Plow	490
2	Fallow Smooth	989
3	Stubble	1627
4	Celery	1127
5	Vineyard Untrained	2891

Table 3: Ground truth classes for the Salinas-B scene and their respective samples number

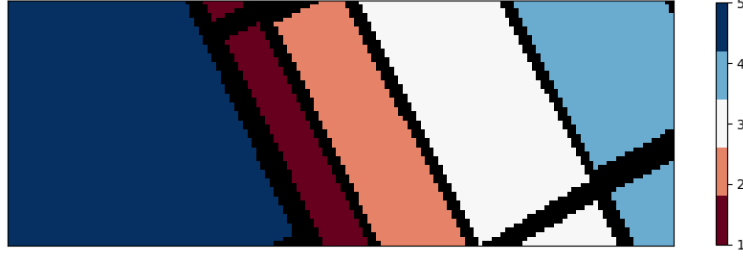


Figure 8: Salinas-B Ground Truth Labels

Using an initial selection of $n_s = 330$ superpixels with shape parameter $m = 2$ and unmixing parameters $\mu = 1$ and $\beta = 0.0025$, a grid search was applied to σ and κ such that $\sigma \in [0.1, 0.001]$ and $\kappa \in [15, 40]$, to which $\sigma = 0.0025$ and $\kappa = 10$ produced the most optimal results with an overall accuracy of 0.998.

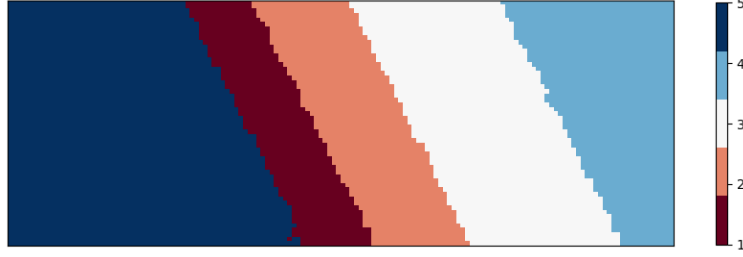


Figure 9: Salinas-B Algorithm Results

	1	2	3	4	5	Accuracy	IoU
1	490	0	0	0	0	1.00	0.992
2	0	989	0	0	0	1.000	1.00
3	0	0	1621	6	0	0.996	0.996
4	0	0	0	1127	0	1.000	0.995
5	4	0	0	0	2887	0.999	0.999

Table 4: Pixel-wise Confusion Matrix (Vertical: Actual, Horizontal: Predicted)

Again, the algorithm itself performs well across all classes, with high individual segment accuracy scores as well as IoU scores, demonstrating it’s ability to perform segmentation in scenarios where similar spectral features are shared among materials and materials span across the image.

4.2.2 Qualitative Evaluation on Samson

Our proposed segmentation algorithm was applied to the Samson A,B and C datasets. While this dataset does not have ground truth labels provided, a qualitative comparison can be performed, with particular focus on noting the ability of the algorithm to distinguish highly mixed pixels along the shorelines of the image and the ability to capture spatial complex segments.

For the Samson datasets, prior knowledge about the scene confirms the aim is to segment the image into $n_e = 3$ segments corresponding to the Water, Dirt and Tree classes. Using an initial selection of $n_s = 961$ superpixels with shape parameter $m = 3$ and unmixing parameters $\mu = 1$ and $\beta = 0.005$, a grid search was applied to σ and κ such that $\sigma \in [0.1, 0.001]$ and $\kappa \in [15, 40]$, to which $\sigma = 0.015$ and $\kappa = 30$ produced the most optimal results in terms of visual coherence with respect to the original image.

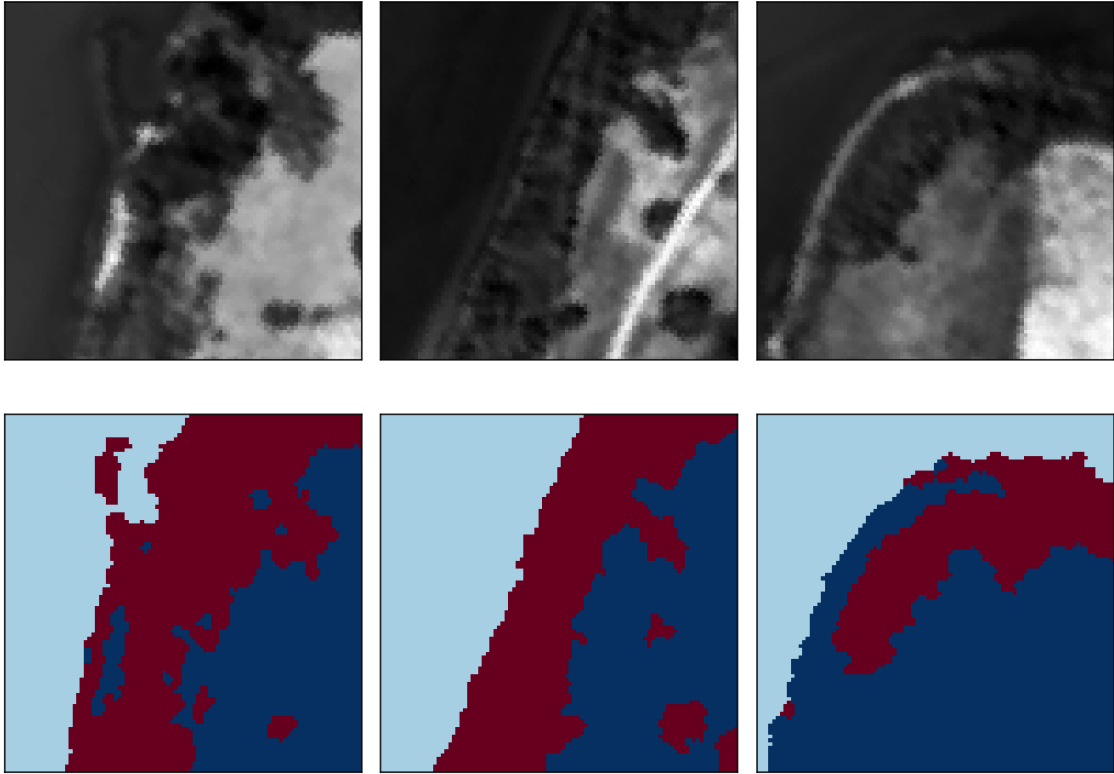


Figure 10: Algorithm Results on Samson (Light Blue is Water, Red is Trees, Dark Blue is Soil)

It can be seen that the algorithm performs well and creates segmentations analogous to the distribution of materials within the scene, with the additional benefit of being able to form noncontinuous structures when the spatial limit κ is set to be higher, allowing more refined segmentation when pockets of materials exist within each other.

5 Conclusions

The proposed algorithm works off the key assumption for future biomedical hyperspectral images that the eye tissues of interest lie in spatially coherent regions and that pixels near each other share similar spectral characteristics. At the heart, a segmentation approach aims to minimize inter segment variance and maximize intrasegment variance. In the context of hyperspectral imaging, the goal of creating accurate segmentations and maximizing accuracy are often the same. As to efficiency directly, the pre clustering step is crucial to allowing an efficient implementation of the graph approach to segmentation. The relaxed normalized cuts approach we implement operates in near cubic time complexity, by selecting a certain average pixel to superpixel ratio, the running time of the algorithm is reduced cubically with respect to a graph approach without superpixel generation.

The experimental results on real-world satellite hyperspectral datasets demonstrate the effectiveness of the proposed approach. It achieves a high degree of accuracy in material identification while having a high degree of flexibility in terms of choices on parameters to produce the final segmentation output. This method offers a valuable tool for researchers and practitioners working in diverse fields that utilize hyperspectral imaging technology in unlabelled scenarios, such as remote sensing and biomedical hyperspectral imaging. Future research directions would be to explore different constructions of the spatial-spectral affinity matrix presented in (27). While the spectral angle metric is useful in many hyperspectral scenarios, the argument can be made that spectral angle alone cannot capture the intricate differences between normalized spectra for certain fields of study, and instead, a mixed of different measures must be considered.

In conclusion, this work presented a novel graph-based segmentation approach that effectively addresses the challenges associated with blind segmentation in hyperspectral images. The proposed method leverages the strengths of both spectral similarity and spatial proximity to achieve accurate segmentation while maintaining computational efficiency. By incorporating the estimated abundance information as a supportive feature, the algorithm refines the segmentation process, leading to superior results in both accuracy and efficacy.

References

- Achanta, R., Shaji, A., Smith, K., Lucchi, A., Fua, P., & Süsstrunk, S. (2012). Slic superpixels compared to state-of-the-art superpixel methods. *IEEE Transactions on Pattern Analysis and Machine Intelligence*, 34(11), 2274–2282. <https://doi.org/10.1109/TPAMI.2012.120>
- Al-Khafaji, S. L., Zhou, J., Bai, X., Qian, Y., & Liew, A. W.-C. (2022). Spectral-spatial boundary detection in hyperspectral images. *IEEE Transactions on Image Processing*, 31, 499–512. <https://doi.org/10.1109/TIP.2021.3131942>
- Boyd, S., Parikh, N., Chu, E., Peleato, B., & Eckstein, J. (2011). Distributed optimization and statistical learning via the alternating direction method of multipliers. *Foundations and Trends in Machine Learning*, 3(1), 1–122. <https://doi.org/10.1561/22000000016>
- Chen, B., Lou, Y., Bertozzi, A. L., & Chanussot, J. (2023). Graph-based active learning for nearly blind hyperspectral unmixing. *IEEE Transactions on Geoscience and Remote Sensing*, 61, 1–16. <https://doi.org/10.1109/TGRS.2023.3313933>
- Condat, L. (2016). Fast projection onto the simplex and the ℓ_1 ball. *Mathematical Programming*, 158(1), 575–585.
- Keshava, N., & Mustard, J. (2002). Spectral unmixing. *IEEE Signal Processing Magazine*, 19(1), 44–57. <https://doi.org/10.1109/79.974727>
- Meerdink, S. K., Hook, S. J., Roberts, D. A., & Abbott, E. A. (2019). The ecostress spectral library version 1.0. *Remote Sensing of Environment*, 230, 111196. <https://doi.org/https://doi.org/10.1016/j.rse.2019.05.015>
- Shi, J., & Malik, J. (2000). Normalized cuts and image segmentation. *IEEE Transactions on Pattern Analysis and Machine Intelligence*, 22(8), 888–905. <https://doi.org/10.1109/34.868688>